Chemical Geology 270 (2010) 249–256

Contents lists available at ScienceDirect

Chemical Geology

journal homepage: www.elsevier.com/locate/chemgeo

Structural study of selenium(IV) substitutions in calcite

G. Aurelio [a,*], A. Fernández-Martínez [b,c], G.J. Cuello [c,d], G. Román-Ross [e], I. Alliot [f], L. Charlet [b]

[a] Conicet and Centro Atómico Bariloche, S. C. de Bariloche, Argentina
[b] LGIT, University of Grenoble-I and CNRS, Grenoble, France
[c] Institut Laue-Langevin, BP 156, F38042 Grenoble, France
[d] Dept. Applied Physics II, UPV/EHU and Ikerbasque, 48080, Bilbao, Spain
[e] Dept. of Chemistry, Faculty of Sciences, University of Girona, Campus Montilivi, 17071, Girona, Spain
[f] CRG-FAME BM30A, European Synchrotron Radiation Facility, Grenoble, France

ARTICLE INFO

Article history:
Received 24 September 2009
Received in revised form 30 November 2009
Accepted 1 December 2009

Editor: J. Fein

Keywords:
Selenium
Calcite
Co-precipitation
Neutron diffraction
EXAFS
DFT modeling

ABSTRACT

In this work we present the results of a crystallographic study of synthetic calcite co-precipitated with selenium. We investigated both at a macroscopic and nanoscopic level, whether Se(IV) can be incorporated to bulk calcite by substitution at carbon sites. Neutron diffraction experiments, EXAFS spectroscopy and a theoretical modeling of the crystallographic structure using VASP are reported. We have found that the calcite unit cell volume obtained from the VASP simulations increases linearly with Se content in the structure. This allows estimating the Se content effectively incorporated into calcite based on volume measurements. Diffraction results are combined with VASP modeling to estimate a concentration of Se(IV) co-precipitated with calcite of 30–75 mmol/kg solid. EXAFS spectroscopy, in combination with our theoretical model of the local structure surrounding the Se atom, confirms the possibility of selenite ion substituting for carbonate anion in the calcite structure.

1. Introduction

Transport of contaminants in the environment may be slowed down by mechanisms such as ion exchange, sorption, or co-precipitation processes. Among these attenuation processes, co-precipitation is a very important retardation mechanism, as it is not limited to the 2D dimension of mineral surfaces, like adsorption. Instead, it may involve the three dimensions of the whole sorbent mineral, and therefore be linked with a much larger sorption capacity for a given sorbent. The retention of toxic ions in mineral phases through this mechanism is relevant in minerals undergoing very dynamic dissolution and re-precipitation processes, such as calcite. During these processes, foreign ions can get trapped into the bulk of a mineral, retarding its transport and subsequent availability in the environment. The ability of a mineral to trap an ion in its bulk structure depends on different physico-chemical aspects like the ion charge, size and structural fit within the mineral structure (Alexandratos et al., 2007; Prieto et al., 2003; Reeder et al., 1994, 2006; Staudt et al., 1994). In some cases, specific adsorption of an ion on a mineral surface can give indications about the possible mechanisms of substitution in the bulk (Alexandratos et al., 2007; Cheng et al., 1999; Roman-Ross et al., 2006). Calcite ($CaCO_3$) is a very common mineral in surface and sedimentary environments. It is therefore of great importance to environmental scientists to gain direct information on the incorporation of ions in calcite, in particular, on the sites and mechanisms of incorporation of different elements and species.

Selenium is known to be a 'double-edged sword' element, having one of the narrowest ranges between dietary deficiency (<40 μg day^{-1} uptake per human body) and toxic levels (>400 μg day^{-1}) (Levander and Burk, 2006). It occurs in natural systems in different oxidation states: selenide (−2), elemental selenium (0), selenite (4+) — Se(IV) — and selenate (6+) — Se(VI). Selenium (IV) and (VI) form oxyanions, which can adopt different protonation states in solution. Selenite is the main species of selenium in many reducing environments, while selenate is more abundant in aerated soils and oxic environments.

Selenium is also present in nuclear waste in the form of ^{79}Se, a fission product of ^{235}U (ANDRA, 2005; Shongsheng et al., 1997) with a half-life of 1.1×10^6 yrs. Because the solubility-limited selenium concentrations with respect to metal selenites are relatively high (pK_s: $FeSeO_3 = 9.99$; $CaSeO_3 = 5.53–7.65$; $K_2SeO_3 = 1.48$; $MnSeO_3 = 6.9–7.11$) (Seby et al., 2001) immobilization mechanisms other than solubility limits are necessary to reduce the ^{79}Se concentration in the nearfield of nuclear waste repositories. These clay–rock environments chosen by various European countries as nuclear waste repositories are characterized, either in the "nearfield" bentonite barrier or in the "farfield" embedding rock, by the presence of calcite and by anoxic conditions. This makes

* Corresponding author. Tel.: +54 2944445180.
E-mail address: gaurelio@cab.cnea.gov.ar (G. Aurelio).

0009-2541/$ – see front matter © 2009 Elsevier B.V. All rights reserved.
doi:10.1016/j.chemgeo.2009.12.004

selenite the dominant species of ^{79}Se upon its release from the nuclear waste and its following oxidative alteration (ANDRA, 2005).

Another source of environmental concern is the point source contamination of local groundwaters by, e.g., fly ash leachates at coal-fired electrical generating station sites. Selenium is among the elements whose concentration is most often observed to be above drinking water standards at these sites (Yudovich and Ketris, 2006). It has been proposed that dolomite [$CaMg(CO_3)_2$] addition to a lime-rich fly ash can reduce the concentrations of selenium, given that, in the presence of portlandite [$Ca(OH)_2$], dolomite undergoes conversion to an assemblage of brucite [$Mg(OH)_2$] and calcite. Therefore, the possible co-precipitation of calcite with selenium may be a mean to reduce its concentration in these environments (Reardon et al., 1993).

Retention of selenium oxyanions at the calcite/water interface has been reported by different authors. Based on electron probe and synchrotron X-ray fluorescence studies, (Staudt et al., 1994) reported a differential incorporation of sulphate (SO_4^{2-}) and selenate (SeO_4^{2-}) at the calcite ($10\bar{1}4$) surface. (Reeder et al., 1994) studied the incorporation mechanism of SeO_4^{2-} within the same surface by Extended X-ray Absorption Fine-structure Spectroscopy (EXAFS), proposing two possible models for the local coordination of SeO_4^{2-} ions. Their results show that even anions with a different geometry like selenate (T_d point symmetry) may be incorporated to the calcite structure in the crystallographic site of carbonate (CO_3, D_{3h} point symmetry).

In this work we present the results of a crystallographic study on synthetic calcite co-precipitated with Se(IV) (selenite, C_{3v} point symmetry) at different concentrations. Our aim is to obtain a mechanistic description of the substitution process at a microscopic scale. For this purpose, we have combined the macroscopic information obtained from wet chemistry and neutron diffraction experiments with the nanoscopic information obtained from EXAFS spectroscopy. In addition, the use of theoretical modelling using ab-initio simulations based on the density functional theory (DFT) has provided valuable information at both the macroscopic and microscopic level, (i) reproducing the macroscopic volume changes associated to the selenite–carbonate substitution, and (ii) providing a theoretical structural model for the local environment of the selenium atom in the calcite bulk structure. This model has been subsequently used as an input for the data treatment of the EXAFS results.

This combined theoretical and experimental approach has been already used in the past to gain information on the calcite bulk properties and to investigate the incorporation of contaminant traces into the calcite and other structures (Cuello et al., 2009; Fernandez-Martinez et al., 2008, 2005; Roman-Ross et al., 2006). The use of neutron diffraction to study bulk properties of minerals is privileged over X-ray diffraction, as neutrons are capable of probing the bulk of materials due to their large penetration depths. At a smaller scale, the EXAFS technique allows exploring selectively the local environment around selenium oxyanions in synthetic calcite samples.

2. Experimental and theoretical methods

2.1. Calcite–Se(IV) co-precipitation

Calcite was precipitated from supersaturated solutions of calcium carbonate prepared by mixing directly into a reactor two equimolar aqueous solutions (0.5 M) of $CaCl_2$ and Na_2CO_3. All chemicals were reagent grade. They were used without further purification and all the solutions were prepared with Milli-Q (18.2 MΩ cm) water. Na_2SeO_3 — Se(IV) — was added to the Na_2CO_3 solution at the beginning of the experiment. The initial concentration of Se(IV) in the reactor ranged from 1×10^{-4} M to 1.2×10^{-3} M. Experimental conditions during precipitation experiments are listed in Table 1.

A reference sample of pure calcite was also prepared. The experiments were carried out at 20 °C and the precipitates were aged for 2 h. The final calcite powder was collected by centrifugation after washing it 3 times with Milli-Q water (18.2 MΩ cm; near-neutral pH). Solids were dried in an oven at 50 °C and subsequently grounded for neutron diffraction analyses. Total chemical analyses of the solids were obtained by ICP-AES (detection limit ~2×10^{-7} mol/L). The resulting Se concentration in the solid for each sample is listed in Table 1. We also measured the Na concentration in sample S3 to discard any possible ion-pair formation between SeO_3 and Na, and obtained a negligible value of [Na] = 0.1408 mmol/kg.

2.2. Neutron diffraction

Neutron diffraction experiments were conducted at the D20 diffractometer of the Institut Laue–Langevin (ILL) in Grenoble, France. This is a two-axis neutron diffractometer with very high flux (~5×10^7 neutrons s^{-1} cm^{-2}). It has a banana-like detector bank composed of 1536 individual micro-strip detectors, covering an angular range of 150°. The samples were placed in vanadium cylindrical containers and each diffractogram was collected during 60–90 min, depending on the amount of sample. The wavelength and the zero angle shift were calibrated with a standard Si sample, yielding a refined wavelength of 1.306 Å and a zero shift of 0.112°. The collected data were corrected by detector efficiency and normalised by monitor counts.

The measured neutron diffractograms were processed with the full-pattern analysis Rietveld method, using the program FullProf (Rodriguez-Carvajal, 1993) for refining the crystal structure. The reference sample of pure calcite was refined assuming the trigonal *R*-3*c* space group with standard atomic positions. Fitted parameters were the lattice constants (*a* and *c*), the *x* coordinate of oxygen atoms and the isotropic thermal constants for each atom. The resulting structure for pure calcite agrees perfectly with that reported in the literature (Maslen et al., 1995) indicative that, although quickly precipitated and finely subdivided, the solid is indeed made of calcite. The same model was then used to refine the data of the selenium-containing samples. As we expected small amounts of selenium being incorporated into the calcite structure, no major changes in the structure factor of calcite were expected, the main changes coming from the expansion of the lattice parameters. For this reason, we refined all the samples without explicitly introducing any Se at the C site, i.e., the occupation of the 6*a* Wyckoff position was always 100% C in the model.

2.3. X-ray absorption spectroscopy

EXAFS spectra of one selected sample (S2) were collected using the fluorescence mode at the BM30 beamline of the synchrotron radiation facilities in Grenoble, France (ESRF) (Proux et al., 2005), using a Si(220) double-crystal monochromator. Multiple scans were taken over the selenium *K*-edge (12658 eV). The sample was held at near 20 K using a liquid He cryostat, which improved the signal/noise ratio. Absorption spectra for the selenium-doped calcite sample were obtained using a germanium 30-element detector.

Table 1
Selenium concentration in the initial solutions used in the co-precipitation experiments, as well as in the solids after the synthesis, measured by ICP-AES.

Sample	Se in solution (mmol/L)	Se in solids (mmol/kg)
S0	0	0
S1	0.1	1.8
S2	1	13.6
S3	5	25.9
S4	12	27.6

Data analysis proceeded by subtraction of a linear pre-edge background, a second-order polynomial post-edge background, normalization, and conversion to k-space, followed by μ_0 fitting using a cubic spline. The $\chi(k)$ function was Fourier transformed using k^2 weighting. All data processing was performed using the Athena software (Ravel and Newville, 2005). The quantitative analyses of EXAFS data were performed using the Artemis software (Ravel and Newville, 2005) based on IFEFFIT. Fits were conducted in the R-space using as input the theoretical model for the selenium local structure obtained from the VASP calculations. The FEFF program in Artemis calculates a theoretical EXAFS spectrum which is composed of individual backscattering paths. Fitting was performed by minimizing the difference between the raw data and our model for FT[$\chi(k)$] from $R=0.8$ to 3.8 Å, being FT[$\chi(k)$] the Fourier transform of the EXAFS function $\chi(k)$ between $k=2.8$ and 13.5 $Å^{-1}$. The minimization proceeded by refining the parameters for each individual path.

2.4. Ab-initio computational simulations

The modeling of the crystallographic structure of Se(IV) incorporated in calcite was performed using ab-initio simulations based on the DFT. The simulations of the ground state energy of the system used the Perdew–Burke–Enzerhof variation of the General Gradient Approximation (GGA) to DFT, as implemented in the VASP Package (Kresse and Hafner, 1993; Kresse and Hafner, 1994). The calculations were performed at the Gamma point ($k=0$), using the provided projector augmented wave (PAW) pseudopotentials with a plane wave cutoff of 280 eV (Kresse and Joubert, 1999). To account for different Se(IV) concentrations, we performed simulations of different supercells of size $m\times n\times l$ unit cells of calcite (30 atoms each) in the a, b and c directions, respectively (m, n, $l=1$, 2 or 3) with one and two SeO_3^{2-} molecules replacing CO_3^{2-} molecules. Different initial conditions were set for each of the calculations: the initial unit cell volume was modified in a range of 5–10 $Å^3$ around the pure calcite value and the location of the replaced CO_3^{2-} molecules was also varied within the cell. This sampling helps to avoid local minima in the energy landscape, and confirms that the results of the simulations do not depend on the initial conditions which can sometimes introduce an undesired bias. Periodic boundary conditions were used to simulate the bulk crystal. Simulations were performed at 0 K. For this reason, the optimized pure calcite unit cell volume is smaller than the experimental value. However, in the present work we shall only discuss relative volume changes which are not affected by this temperature shift.

3. Results and discussion

3.1. Selenium speciation and precipitation experiments

The fate of selenium in natural environments is controlled by its speciation. The more oxidized selenium species are generally most soluble. Selenate is the most soluble species, followed by selenite, which sorbs strongly onto iron oxide surfaces (Duc et al., 2003), clay minerals (BarYosef and Meek, 1987; Charlet et al., 2007; Frost and Griffin, 1977; Peak et al., 2006), soil organic matter (Gustafsson and Johnsson, 1994; Tam et al., 1995) and calcite (Reeder et al., 1994). Redox transformations produce changes in the selenium speciation and, therefore, in the molecular geometry of selenium oxyanions (Fernandez-Martinez and Charlet, 2009). In solution, the selenite (SeO_3^{2-}) molecule assumes a pyramidal–trigonal shape (C_{3v} symmetry), whereas selenate (SeO_4^{2-}) presents a tetrahedral shape (T_d symmetry), as sketched in Fig. 1(a) and (b). The species under study is a molecular ion, with a three-dimensional structure, and therefore its incorporation to mineral surfaces or bulk needs to take into account not only charge balance but also the atomic-scale structure of the molecules.

Among the four synthetic samples of Se-doped calcite, all of them except S4 resulted in the crystallization of calcite. This was confirmed by scanning electron microscopy and X-ray diffraction (data not shown). No other phases were detected in these samples. In Fig. 2 we show a selection of scanning electron micrographs for samples S1, S2, S3 and S4, synthesized in the presence of Se(IV). We observe well defined calcite crystallites with a smooth surface and similar size distribution. Nevertheless, at higher Se(IV) concentrations the precipitation of calcite is suppressed and other polymorphs of $CaCO_3$ crystallize, as is the case of vaterite shown in Fig. 2(d).

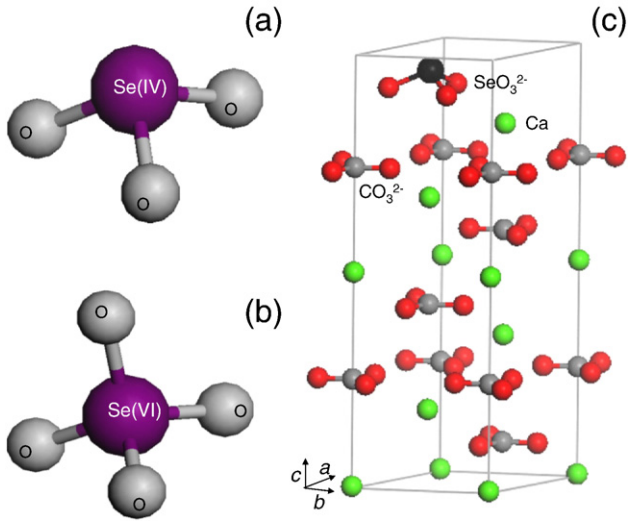

Fig. 1. Molecular geometry of selenite (SeO_3^{2-}) (a) and selenate (SeO_4^{2-}) (b) oxyanions in solution. (c) Simulated incorporation of a selenite unit SeO_3^{2-} in the calcite unit cell. In the initial stage of the simulation the Se atom (black) was placed at a carbon site (in a planar configuration) and evolved into a pyramidal configuration.

3.2. Diffraction results

Except for sample S4, the neutron diffraction refinements were successfully conducted using the calcite structure and present an excellent quality, with average reliability factors $R_p=2.5$ and $R_{wp}=3$. In Fig. 3 we present the refined neutron diffractograms for samples S2 and S4. Symbols correspond to the neutron diffraction data and the solid line represents the refinement. The line at the bottom indicates the difference between the calculated and observed patterns. The shape of the background for sample S2 is an indication that the powder was not completely dry but does not interfere with the refinement of the crystalline phase. The refinement for sample S0, corresponding to pure calcite, is in perfect agreement with data for calcite reported in the literature (Maslen et al., 1995). On the other hand, the structure of sample S4 proved to be not calcite but mostly vaterite, as shown in the bottom panel of Fig. 3. In Table 2 we present a summary of the lattice constants refined for each calcite sample.

3.3. Modeling results

For the theoretical calculations, several initial models were prepared, in which CO_3^{2-} units were substituted by selenite units SeO_3^{2-} forced at a planar configuration, keeping the same overall geometry of pure calcite. In all cases, after the VASP optimizations, these artificially planar SeO_3^{2-} units evolved to a state of minimal energy in which the Se atom pops out of the CO_3 planes of calcite, forming a pyramid with its three neighbouring oxygen atoms at the base. This shape is characteristic of the Se(IV) species in solution, and had also already been reported both from theoretical and experimental studies for the substitution of As(III) in calcite (Roman-Ross et al., 2006). It is interesting to note that the base of the pyramid, composed of three oxygens, remains in the same plane as the original

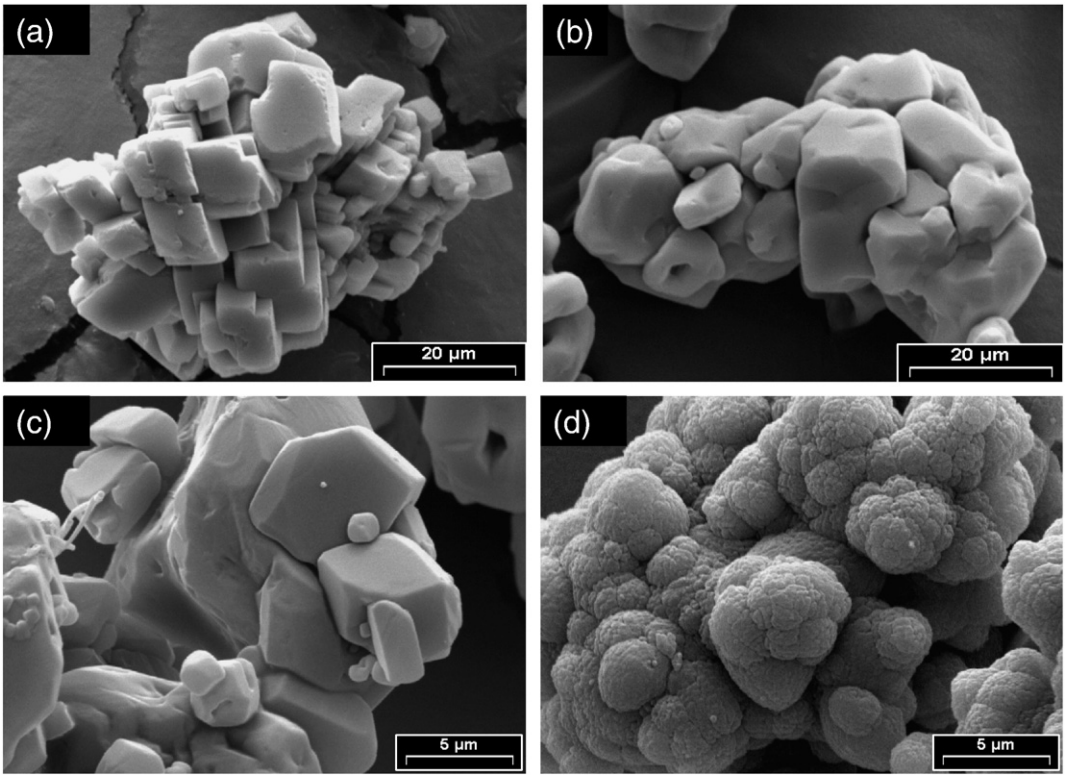

Fig. 2. Scanning electron micrographs of calcite samples S1(a), S2(b) and S3(c); and sample S4(d) corresponding to the vaterite polymorph of $CaCO_3$.

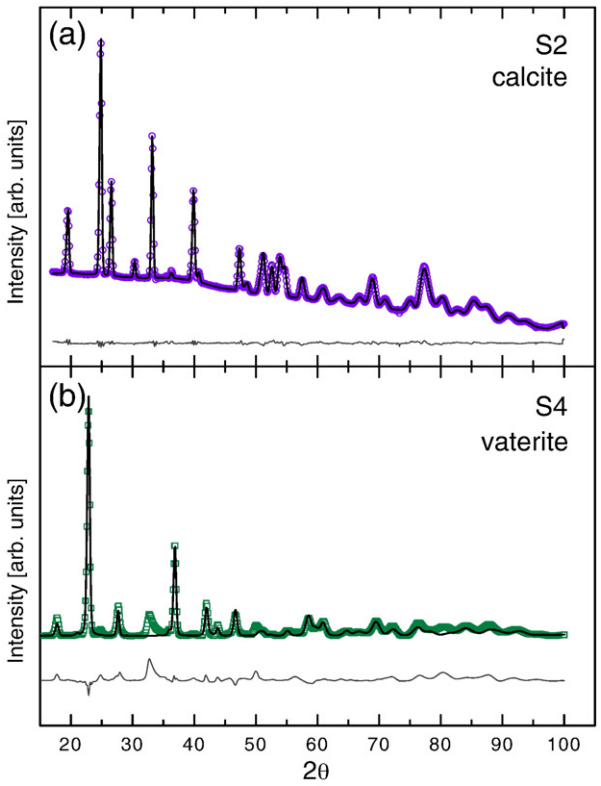

Fig. 3. Rietveld refinements of the neutron diffraction data for samples S2(a), showing the calcite structure, and S4(b) showing the vaterite structure. Symbols represent experimental data; the solid line corresponds to the refinement. The line at the bottom of each graph indicates the difference between observed and calculated patterns.

CO_3^{2-} unit, as assumed by (Cheng et al., 1997) in their X-ray Standing Wave study of selenite absorption on calcite surface. The resulting structure from our simulations is shown in Fig. 1(c).

To study the theoretical volume changes associated with the incorporation of Se(IV), we modeled different supercells and Se concentrations according to Table 3. One calcite unit cell corresponds to 6 units of $CaCO_3$, each with a molecular mass M_{CaCO3} (100.09×10^{-3} kg/mol). The concentration of Se in the solid is calculated as:

$$[Se] = y^{*}m_{Se} / M_{supercell}\,[\text{kg Se/kg solid}]$$

$$= y^{*}1 \times 10^{3} / M_{supercell}\,[\text{mmol Se/kg solid}]$$

where y denotes the total number of C atoms ($m_C = 12.011\times10^{-3}$ kg/mol) replaced by Se ($m_{Se} = 78.96\times10^{-3}$ kg/mol) in the supercell and $M_{supercell}$ is computed as the total atomic mass of the given $m\times n\times l$ supercell,

$$M_{supercell} = m^{*}n^{*}l^{*}6^{*}M_{CaCO3} - y^{*}m_C + y^{*}m_{Se}.$$

The values used in our simulations for y, n, m and l are listed in Table 3.

In Fig. 4 we present the effect of the Se(IV) replacement on the volume of the optimized unit cells, as a function of Se concentration. For each concentration, the series of symbols represent runs conducted with different initial conditions and/or different supercells. The results in

Table 2
Results from the Rietveld refinement of neutron diffraction data. Lattice parameters, volume of the unit cell and relative volume expansion with respect to pure calcite are indicated.

Sample	a [Å]	c [Å]	V [Å^3]	$\Delta V/V_0$ [10^{-4}]
S0	4.990(1)	17.069(2)	368.1(2)	0
S1	4.9926(3)	17.069(1)	368.46(6)	8(4)
S2	4.9922(3)	17.070(1)	368.42(6)	7(4)
S3	4.9927(3)	17.073(1)	368.56(6)	11(4)

Table 3
List of all the simulated supercells of size $m \times n \times l$ unit cells of calcite in the *a*, *b* and *c* directions, respectively, and their corresponding selenium concentration values.

Supercell			Number of replaced atoms	Selenium concentration [mmol/kg solids]
n	*m*	*l*	*y*	[Se]
1	1	1	0	0
2	2	1	0	0
2	2	2	0	0
3	2	1	0	0
1	1	1	1	1498.2
2	1	1	2	1498.2
2	1	1	1	788.6
3	2	1	2	535.2
2	2	1	1	405
3	2	1	1	272.5
2	2	2	1	205.3

Fig. 4 show an expansion of the unit cell volume proportional to the Se concentration, following a linear Vegard's law behavior (solid line). To investigate size effects in the simulations, we also performed the optimization of pure calcite using different supercells. The results are shown in the inset of Fig. 4 We observe a very slight increase in the optimized volume as the number of atoms in the simulation box increases, which may be taken as an indicative of the uncertainty bars of the simulated volumes due to size effects (smaller than the symbol sizes in Fig. 4), in addition to the uncertainty coming from the scatter at each concentration due to different initial conditions. In this graph, we also show the experimental volume for pure calcite (Maslen et al., 1995) at room temperature for comparison (solid symbol). However, as the simulations were performed at 0 K, it is better to represent the expansion in terms of relative changes. The relative volume expansion of the calcite unit cell as a function of Se addition is shown in Fig. 5. Each point represents the average value of the set of samples optimized at each concentration in Fig. 4. The reference volume V_0 was taken as the average volume for our simulated pure calcite cell. The line in Fig. 5 represents a linear fit to the data constrained to the value $\Delta V/V_0 = 0$ for [Se] = 0, where [Se] represents the selenium concentration in mmol/kg of solid. The fit yields

$$\Delta V / V_0 = 1.80(3) \times 10^{-5} \times [Se] \quad (1)$$

The potential of this fit is to allow an estimate of the amount of Se actually incorporated to the bulk of calcite, based on an experimentally

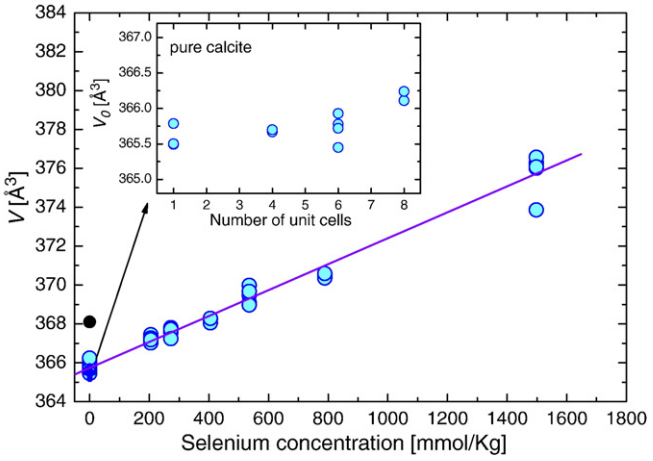

Fig. 4. Volume expansion of the simulated calcite unit cell as a function of selenium concentration. The experimental volume of pure calcite at room temperature is indicated by a black solid circle. The solid line represents a linear fit to all the simulated data. The inset shows how the size of the simulation cell affects the unit cell volume in pure calcite.

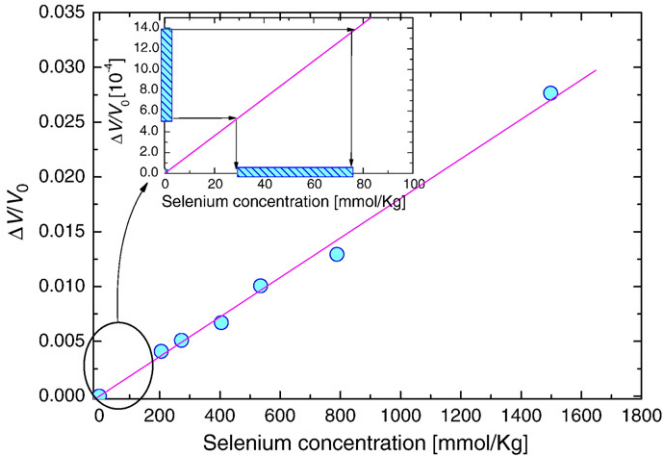

Fig. 5. Theoretical relative volume expansion as a function of selenium concentration. V_0 corresponds to the average pure calcite simulated volume. The line represents a linear fit to the data. In the inset, the low-selenium region is zoomed. The hatched area in the ordinate axis corresponds to the range of experimental $\Delta V = V_0$ values coming from neutron diffraction experiments. The hatched area in the abscissa axis corresponds to the extrapolated range of selenium concentrations incorporated into the structure in the co-precipitation experiments.

determined volume expansion in relation to the pure calcite volume V_0. To this end, we have calculated the experimental $\Delta V/V_0$ values coming from our neutron diffraction experiments. They are presented in the last column of Table 2. Although of low precision, the values corresponding to Se(IV) samples can be used as a reference to be introduced in Eq. (1) to get an estimate of the concentration of Se actually incorporated. The range of experimental $\Delta V/V_0$ values has been hatched in the ordinate axis of the inset in Fig. 5. Following the arrows, we arrive at a range of possible Se concentrations between 30 and 75 mmol/kg of solid, hatched in the abscissa axis, a range which is in the same order of magnitude as the experimental Se concentrations in the solids measured by ICP-AES.

It must be emphasized that based on wet chemical experiments, the range of possible Se trapping in calcite is always on the low-concentrated region of these graphs (Figs. 4 and 5). For more concentrated values, pure Calcium Selenate or Calcium Selenite solid phases are thermodynamically expected to precipitate (pK_s of $CaSeO_3.H_2O$ has been estimated at 6.84 to 7.27, (Baur and Johnson, 2003)). Therefore, it is expected that the actual local environment of the Se atom in calcite is better represented by the largest simulation cells. However, as the computational cost increases with larger simulation sizes, it is important to obtain estimates for the low concentration range from smaller and faster simulation conditions. We can see from our simulations that the average Se–O distance is indeed almost size-independent.

With these results, we arrive at a local structural model around a Se(IV) atom in calcite which can in turn be used as a theoretical input for the analysis of EXAFS experiments. The model is presented in Fig. 6, from two different perspectives. Panel (a) corresponds to a projection along the *y* direction, where we can see the stacking sequence of CO_3 units and Ca planes. In panel (b) we show a projection along the *z* direction to visualize the rotation between units. One should remember, in the following, that the simulations have been performed using the PBE–GGA functional, which is known to slightly overestimate inter-atomic bond lengths (Menconi and Tozer, 2002). For this reason a slight shift with respect to experimental distances obtained from EXAFS data is to be expected.

3.2. XAS spectroscopic results

X-ray absorption spectroscopy at the Se K-edge (12,658 eV) has been used to characterize the local structure and coordination of

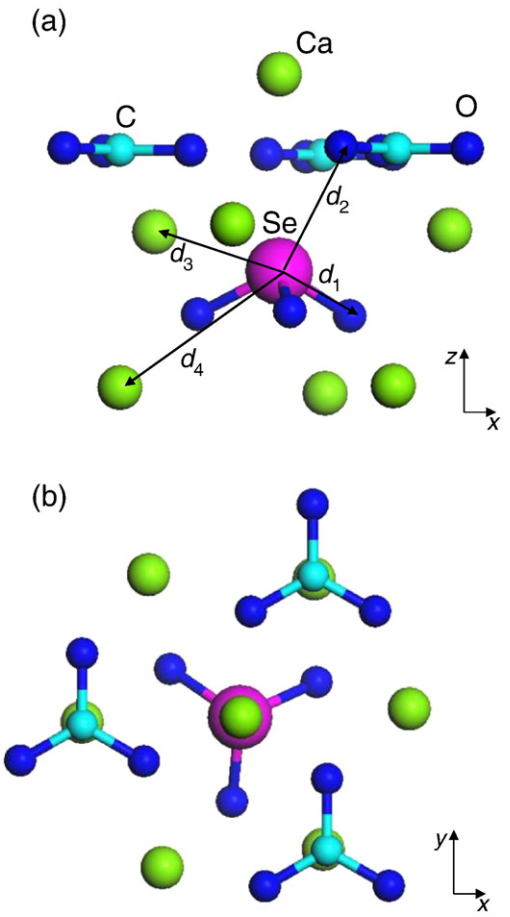

Fig. 6. Local structure around a Se(IV) atom in calcite, resulting from the VASP simulations. Panel (a) corresponds to a projection along the *y* direction and panel (b) to the projection along the *z* direction. The relevant distances to the nearest shells around the Se atoms are indicated by arrows.

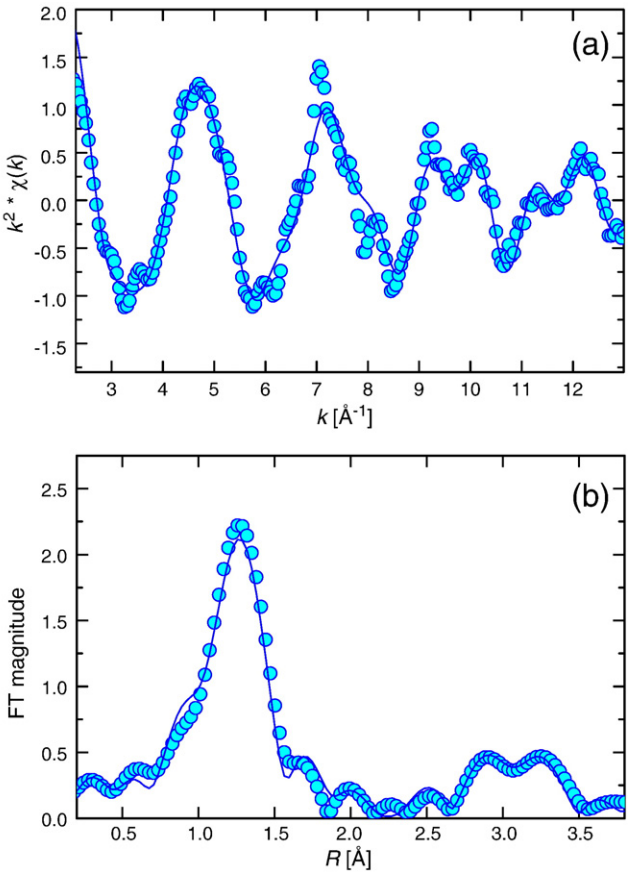

Fig. 7. EXAFS results for selenite incorporated in sample S2. Symbols denote raw data and solid lines correspond to the fits to our model based on VASP simulations. The top panel (a) corresponds to the k^2-weighted $\chi(k)$ function and the bottom panel (b) represents the Fourier transform magnitude of $k^2\chi(k)$.

selenium co-precipitated with calcite starting from room temperature aqueous solutions containing Se(IV). The X-ray Absorption Near Edge Structure (XANES) spectra provide information on the actual oxidation state of Se in the solid. In addition EXAFS reveals the short range order around the selenium atom. In this work we have used both techniques. The obtained spectra for our calcite sample is consistent in shape and position with the XANES of an aqueous SeO_3^{2-} solution (Peak et al., 2006), confirming that in these samples Se is present as Se(IV).

After extracting the EXAFS signal from the spectrum, fits were conducted in the *R*-space using as input the theoretical model for the local structure around Se obtained from our VASP calculations, as discussed in Section 3.1. Four scattering paths were considered in the fits, corresponding to single scattering paths between the central Se atom and a first and second shell of O atoms, and a third and fourth shell of Ca atoms. The local structure around Se in our model consists of two O shells of 3 atoms each, at distances d_1 and d_2; and two Ca shells of 3 atoms each, located at d_3 and d_4, as sketched in Fig. 6. These distances, as well as the coordination numbers and other parameters, are allowed to vary during the fits to minimize the difference between the EXAFS data and the EXAFS equation based on our model.

In Fig. 7 we present the results of the EXAFS fits. The upper panel corresponds to the k^2-weighted $\chi(k)$ function and the bottom panel represents the Fourier transform magnitude of $\chi(k)$. Sample S2 presents features consistent with more than just one shell of atoms surrounding Se. In this kind of studies, the absence/presence of calcium backscatterers and a well defined structure beyond the first shell provide insight into the degree of disorder associated with disruption of the local calcite structure, and can be taken as indicative of the inability/ability of the contaminant unit to assume a stable structural environment in the host calcite. The Fourier transform magnitude of $\chi(k)$ in Fig. 7 shows a well defined local structure around Se, which is fully compatible with our VASP model, in which Se is effectively incorporated into the calcite structure.

The parameters optimized in the fits are summarized in Table 4. From the results in Table 4, we can see that the possibility of fitting three more shells around Se, in good agreement with our structural calculated model, constitutes clear evidence that calcite has effectively incorporated Se as Se(IV). Moreover, we have considered other possible environments for the Se atom in our sample, which could result in a similar EXAFS signal. The precipitation of calcium selenite $CaSeO_3.2H_2O$ was discarded for several reasons: the solutions used were undersaturated with respect to this phase, our neutron diffraction data show no evidence of precipitation of a second phase other than calcite, and eventually, the inter-atomic distances in $CaSeO_3 \cdot 2H_2O$ differ from the ones obtained in our fits (Valkonen, 1986; Valkonen et al., 1985).

Table 4
Structural parameters obtained by fitting our VASP model to the EXAFS data for sample S2. The shells indicated in the first column correspond to those sketched in Fig. 6.

Sample S2	CN	R [Å]	σ^2 [Å^2]	E_0 [eV]	R_{VASP} [Å]
Se–O (d_1)	2.8(5)	1.67(1)	0.002(1)	5(3)	1.727
Se–O (d_2)	1(1)	2.87(8)	0.002(1)	9(7)	2.876
Se–Ca (d_3)	1.3(8)	3.25(3)	0.002(1)	12(7)	3.202
Se–Ca (d_4)	1.7(9)	3.53(4)	0.002(1)	12(7)	3.565

4. Conclusions

In the present study calcite is shown to be able to host up to 27.6 mmol Se/kg of solid within its structure, by a nearly isomorphic substitution of carbonate ions by selenite ions. This was demonstrated using neutron diffraction experiments, in which we tested whether the volume expansion of the calcite unit cell could be indicative of the contaminant incorporation. Furthermore, we have modeled several crystallographic arrangements to evaluate the substitution of Se for different supercells (concentrations), using the DFT-based simulation package VASP. Finally, we have used the obtained theoretical model for the local structure around Se in the bulk of calcite to successfully analyze an EXAFS spectrum, confirming the incorporation of Se(IV) into calcite. The calcite unit cell volume obtained from the VASP simulations increases linearly with Se content in the structure, a further indication of the formation of a solid solution. This clear trend allows estimating the Se(IV) content effectively incorporated based on unit cell volume measurements. We used the neutron diffraction technique to explore the macroscopic volume expansion associated to the incorporation of Se(IV), since neutrons penetrate deeply into calcite and probe the bulk mineral more efficiently than X-rays. Our results from diffraction measurements excluded the possibility to have selenium present in a secondary precipitated phase. Diffraction results were combined with our DFT modeling to predict a Se(IV) incorporation in the 30 to 75 mmol/kg concentration range. Although these values fall in a range slightly higher than the values measured by ICP-OES, they are in the same order of magnitude as the experimental data. The low values of the volume expansion measured experimentally make difficult to obtain reliable values of the actual Se concentration from the calculations. However, the close values obtained by the two methods and the linear Vegard's law observed in the calculations allow interpreting this small volume expansion as the result of selenite incorporation in the bulk of calcite. The most powerful tool to show that co-precipitation process actually occurred was found to be the EXAFS spectroscopy, in combination with our theoretical model of the local structure surrounding the Se atom. We demonstrate the occurrence of four atomic shells surrounding Se, an indication of highly ordered impurity incorporation into calcite.

This study shows that selenite ions may substitute for carbonate anions in the calcite structure. Therefore, in case of contamination of an anoxic aqueous phase by selenium (e.g. ^{79}Se), calcite represents an extremely large sink for selenium because of its dynamic solubility equilibrium, even if only present in trace amounts as is the case in shales or clay rocks, given its ability to trap selenite ions within its structure during the dissolution/precipitation cycles going on even in conditions close to equilibrium.

Acknowledgements

The authors thank Dr. F. Bardelli for fruitful discussions on the EXAFS technique and for providing Se standards, and Delphine Tisserand for her help with the ICP-OES analyses. G.A. acknowledges financial support from ANPCyT under project PICT38024/05, Carlos Cotaro and Ernesto Scerbo for their help with the SEM images. Partial financial support for this research by the EU project RECOSY is also acknowledged. GRR thanks the Spanish Minister of Science and Innovation and the Ramón y Cajal Programme.

References

Alexandratos, V.G., Elzinga, E.J., Reeder, R.J., 2007. Arsenate uptake by calcite: macroscopic and spectroscopic characterization of adsorption and incorporation mechanisms. Geochimica et Cosmochimica Acta 71 (17), 4172–4187.

ANDRA, 2005. Dossier 2005 Argile. Evaluation de surete du stockage geologique. Agence National pour la gestion des Dechets Radioactifs, Paris.

BarYosef, B., Meek, D., 1987. Selenium sorption by kaolinite and montmorillonite. Soil Science 144 (1), 11–19.

Baur, I., Johnson, C.A., 2003. Sorption of selenite and selenate to cement minerals. Environmental Science & Technology 37 (15), 3442–3447.

Charlet, L., et al., 2007. Electron transfer at the mineral/water interface: selenium reduction by ferrous iron sorbed on clay. Geochimica Et Cosmochimica Acta 71 (23), 5731–5749.

Cheng, L.W., Lyman, P.F., Sturchio, N.C., Bedzyk, M.J., 1997. X-ray standing wave investigation of the surface structure of selenite anions adsorbed on calcite. Surface Science 382 (1–3), L690–L695.

Cheng, L.W., Fenter, P., Sturchio, N.C., Zhong, Z., Bedzyk, M.J., 1999. X-ray standing wave study of arsenite incorporation at the calcite surface. Geochimica et Cosmochimica Acta 63 (19–20), 3153–3157.

Cuello, G.J., et al., 2009. Pollutant speciation in water and related environmental treatment issues. In: Liang, L., Rinaldi, R., Schober, H. (Eds.), Neutron applications in Earth, Energy and Environmental Sciences. Neutron scattering applications and techniques. Springer Ed.

Duc, M., et al., 2003. Sorption of selenium anionic species on apatites and iron oxides from aqueous solutions. Journal of Environmental Radioactivity 70 (1–2), 61–72.

Fernandez-Martinez, A., Charlet, L., 2009. Selenium bioavailability and cycling in the environment: a structural chemist point of view. Reviews in Environmental Science and Biotechnology 8, 81–110.

Fernandez-Martinez, A., et al., 2005. Arsenic uptake by gypsum and calcite: modelling and probing by neutron and X-ray scattering. Physica B: Condensed Matter 385–386, 935–937.

Fernandez-Martinez, A., et al., 2008. Arsenate incorporation in gypsum probed by neutron, X-ray scattering and density functional theory modeling. Journal of Physical Chemistry A 112 (23), 5159–5166.

Frost, R.R., Griffin, R.A., 1977. Effect of Ph on adsorption of arsenic and selenium from landfill leachate by clay-minerals. Soil Science Society of America Journal 41 (1), 53–57.

Gustafsson, J.P., Johnsson, L., 1994. The association between selenium and humic substances in forested ecosystems — laboratory evidence. Applied Organometallic Chemistry 8 (2), 141–147.

Kresse, G., Hafner, J., 1993. Ab-initio molecular dynamics for liquid metals. Physical Review B 47 (1), 558–561.

Kresse, G., Hafner, J., 1994. Ab-initio molecular dynamics simulation of the liquid–metal amorphous semiconductor transition in germanium. Physical Review B 49 (20), 14251–14269.

Kresse, G., Joubert, D., 1999. From ultrasoft pseudopotentials to the projector augmented-wave method. Physical Review B 59 (3), 1758–1775.

Levander, O.A., Burk, R.F., 2006. Update of human dietary standards for selenium, selenium. Its Molecular Biology and Role in Human Health. Springer US, New York, pp. 399–410.

Maslen, E.N., Streltsov, V.A., Streltsova, N.R., Ishizawa, N., 1995. Electron density and optical anisotropy in rhombohedral carbonates.3. Synchrotron X-ray studies of $CaCO_3$, $MgCO_3$ and $MnCO_3$. Acta Crystallographica Section B-Structural Science 51, 929–939.

Menconi, G., Tozer, D.J., 2002. Diatomic bond lengths and vibrational frequencies: assessment of recently developed exchange–correlation functionals. Chemical Physics Letters 360 (1–2), 38–46.

Peak, D., Saha, U.K., Huang, P.M., 2006. Selenite adsorption mechanisms on pure and coated montmorillonite: an EXAFS and XANES spectroscopic study. Soil Science Society of America Journal 70 (1), 192–203.

Prieto, M., Cubillas, P., Fernandez-Gonzalez, A., 2003. Uptake of dissolved Cd by biogenic and abiogenic aragonite: a comparison with sorption onto calcite. Geochimica et Cosmochimica Acta 67 (20), 3859–3869.

Proux, O., et al., 2005. FAME: a new beamline for X-ray absorption investigations of very-diluted systems of environmental, material and biological interests. Physica Scripta T115, 970–973.

Ravel, B., Newville, M., 2005. ATHENA, ARTEMIS, HEPHAESTUS: data analysis for X-ray absorption spectroscopy using IFEFFIT. Journal of Synchrotron Radiation 12, 537–541.

Reardon, E.J., Warren, C.J., Hobbs, M.Y., 1993. Reduction of trace-element concentrations in alkaline waste porewaters by dedolomitization. Environmental Science & Technology 27 (2), 310–315.

Reeder, R.J., Lamble, G.M., Lee, J.F., Staudt, W.J., 1994. Mechanism of SeO_4^{2-} substitution in calcite — an XAFS study. Geochimica Et Cosmochimica Acta 58 (24), 5639–5646.

Reeder, R.J., Schoonen, M.A.A., Lanzirotti, A., 2006. Metal speciation and its role in bioaccessibility and bioavailability. In: Sahai, N., Schoonen, M.A.A., Skinner, H.C.W. (Eds.), The Emergent Field of Medical Mineralogy and Geochemistry. Reviews in Mineralogy and Geochemistry. Mineralogical Society of America and the Geochemical Society, USA, pp. 59–113.

Rodriguez-Carvajal, J., 1993. Recent advances in magnetic structure determination by neutron powder diffraction. Physica B 192, 55.

Roman-Ross, G., Cuello, G.J., Turrillas, X., Fernandez-Martinez, A., Charlet, L., 2006. Arsenite sorption and co-precipitation with calcite. Chemical Geology 233 (3–4), 328–336.

Seby, F., Potin-Gautier, M., Giffaut, E., Borge, G., Donard, O.F.X., 2001. A critical review of thermodynamic data for selenium species at 25 degrees C. Chemical Geology 171 (3–4), 173–194.

Shongsheng, J., et al., 1997. Determination of the half-life of ^{79}Se with the accelerator mass spectrometry technique. Nuclear Instruments and Methods B 123 (1–4), 405–409.

Staudt, W.J., Reeder, R.J., Schoonen, M.A.A., 1994. Surface structural controls on compositional zoning of SO_4^{2-} and SeO_4^{2-} in synthetic calcite single-crystals. Geochimica et Cosmochimica Acta 58 (9), 2087–2098.

Tam, S.C., Chow, A., Hadley, D., 1995. Effects of organic-component on the immobilization of selenium on iron oxyhydroxide. Science of the Total Environment 164 (1), 1–7.

Valkonen, J., 1986. Crystal structures, infrared spectra and thermal behavior of calcium hydrogenselenite monohydrate, $Ca(HSeO_3)2\cdot H_2O$, and dicalcium diselenite bis (hydrogenselenite), $Ca_2(HSeO_3)2(Se_2O_5)$. Journal of Solid State Chemistry 65 (3), 363–369.

Valkonen, J., Losoi, T., Pajunen, A., 1985. Structure of calcium selenite(IV) monohydrate, $CaSeO_3$ H_2O. Acta Crystallographica Section C-Crystal Structure Communications 41, 652–654 MAY.

Yudovich, Y.E., Ketris, M.P., 2006. Selenium in coal: a review. International Journal of Coal Geology 67 (1–2), 112–126.